



Superionically Conducting β'' -Al₂O₃ Thin Films Processed Using Flame Synthesized Nanopowders

Journal:	<i>Journal of Materials Chemistry A</i>
Manuscript ID	TA-ART-03-2018-002907.R1
Article Type:	Paper
Date Submitted by the Author:	03-Jun-2018
Complete List of Authors:	YI, EONGYU; University of Michigan, Materials Science and Engineering Temeche, Eleni; The University of Michigan, Materials Science and Engineering Laine, Richard; The University of Michigan, Macromolecular Science and Engineering Center



ARTICLE

Received 00th January 20xx,

Superionically Conducting β'' -Al₂O₃ Thin Films Processed Using Flame Synthesized Nanopowders

Eongyu Yi,* Eleni Temeche, and Richard M. Laine*

Accepted 00th January 20xx

DOI: 10.1039/x0xx00000x

www.rsc.org/

Commercial β'' -Al₂O₃ solid electrolytes for Na⁺ batteries are exclusively produced in tubular form, in part, due to processing difficulties. High sintering temperatures combined with Na₂O loss and excessive grain growth complicate processing of β'' -Al₂O₃ thin films (<100 μ m) which could potentially reduce cell resistance, increase energy density, and even permit room temperature operations. In this study, we use high surface area flame made nanopowders at selected compositions to drive densification to produce β'' -Al₂O₃ thin films with controlled microstructures and Na₂O loss to maintain a high β'' -Al₂O₃ fraction. We show that addition of TiO₂ and ZrO₂ dramatically enhances the sintering kinetics, resulting in dense (>95 %), thin (\leq 50 μ m) β'' -Al₂O₃ films at the lowest sintering temperature ever reported (1320 °C/2 h). The sintered films also offer superionic conductivity (>1 mS cm⁻¹) at room temperature. Symmetrical cell (Na/ β'' -Al₂O₃/Na) testing further confirms its potential utility in Na batteries using β'' -Al₂O₃ solid electrolytes.

Introduction

Sodium β'' -Al₂O₃ has been the subject of numerous studies for the last 50 years because of its utility and potential utility as a Na⁺ conductor for a variety of applications including batteries, thermal electric generators, as well as a number of different types of high temperature fuel cells.¹⁻¹¹ The successful use of β'' -Al₂O₃ for any of these applications mandates optimization of its properties as an efficient Na⁺ conductor but also as a mechanically robust ceramic able to endure the rapid temperature extremes encountered in some of the more demanding applications.¹²⁻¹⁴

In general, it is now well recognized that β'' -Al₂O₃ offers better Na⁺ transport properties than the very similar β -Al₂O₃; thus, multiple work has focused on optimizing processing towards this goal employing a variety of approaches. Among them, researchers have used: solid-state reactions; tape casting, microwave, combustion, and sol-gel syntheses.¹⁵⁻²³ In addition, to optimize the utility of β'' -Al₂O₃, a variety of structural formats have been explored beginning with simple pellets, tape cast films, and tubes targeting tubular battery and thermoelectric conversion devices.^{15,17,19,23-26}

β'' -Al₂O₃ tubes are commonly produced by solid-state reaction in which starting powders are repeatedly ball-milled and calcined, then sintered to obtain the desired microstructural, physical, and electrochemical properties. Common sintering conditions involve heating to \geq 1600 °C for 0.5-4 h causing Na₂O to rapidly volatilize such that the green bodies are covered in a β'' -Al₂O₃ powder bed or placed in a container to minimize Na₂O loss. Na₂O loss during sintering results in formation of less conductive β -Al₂O₃.⁷ Furthermore, the high sintering temperatures cause excessive grain growth leading to 50-500 μ m sized grains which exacerbate mechanical properties.^{6,27}

In many instances, optimization of Na⁺ conductivity was achieved through introduction of dopants including, Li⁺, Mg²⁺, Ti⁴⁺, Mn⁴⁺, or secondary phases of ZrO₂ and Y:ZrO₂ (YSZ).^{4,12,14,21} In part these stabilize the β'' structure, in part they limit excessive grain growth and in part they provide mechanical strength to the final sintered β'' -Al₂O₃ structures.

Good microstructural control has been achieved by vapor phase processing in which α -Al₂O₃/YSZ (70:30 vol.%) composites are sintered to high densities at 1600 °C/2 h, then reheated to 1400 °C with the samples covered in β'' -Al₂O₃ until full conversion of α -Al₂O₃ to β'' -Al₂O₃ is reached.²⁸ The final grain size is equal to the initial grain size prior to conversion but requires multiple heating steps and high YSZ fractions which lowers the overall conductivity.

Simply put, facile processing routes to high density β'' -Al₂O₃ films with fine microstructural control at low sintering temperatures remains problematic. Furthermore, most studies involve sintering powder compacts or thick tubes that are not suitable for producing thin films. Only a few reports concern relatively thin (100-300 μ m) free standing plates or at 50 μ m but as a coating on a porous tube.^{20,24}

At present, commercial Na⁺ batteries use 1-2 mm thick β'' -Al₂O₃ tubular electrolytes that also offer the necessary mechanical framework.⁵ Processing difficulties have limited this material to such forms. As a result cells must operate at 300-350 °C where the electrolyte resistance drops but in fact is still roughly half of the entire cell due to the required thickness.^{5,6} If β'' -Al₂O₃ thin films (< 100 μ m) with optimal properties can be achieved, novel cell designs in flat geometries and even room temperature operation may be realized. Indeed, Liu et al. recently reported room temperature operation of all-solid-state Na⁺ batteries using β'' -Al₂O₃ electrolyte but at thickness of 500 μ m.²⁹ The world-wide demand for Li suggests fundamental limitations to total Li resources that are anticipated to result in cost increases. Consequently, Na batteries offer a low cost, environmentally friendly alternative.^{5,8}

Materials Science and Engineering, University of Michigan, Ann Arbor, MI, 48109

*Corresponding author. Tel.: +1 734 764-6203

E-mail address: talsdad@umich.edu

Here, we demonstrate the advantages of nanopowder (NP) processing, using high surface area, flame made β'' -Al₂O₃ NPs. We coincidentally introduce TiO₂ and ZrO₂ NP dopants at selected concentrations and use various sintering temperatures to optimize densification behavior and conductivities. Sintered β'' -Al₂O₃ films were characterized by XRD, SEM, Archimedes and EIS. A symmetrical Na/ β'' -Al₂O₃/Na cells was also processed for preliminary testing.

Experimental

Precursor synthesis and powder production

Sodium propionate [NaO₂CCH₂CH₃] was synthesized by reacting sodium hydroxide (80 g, 2 mole) with propionic acid (445 g, 6 mole) in a 1 L round bottom flask equipped with a still head at 130 °C in N₂ atmosphere. Once transparent liquid was obtained, heat was removed and sodium propionate crystallized on cooling which was filtered off. Magnesium propionate [Mg(O₂CCH₂CH₃)₂] was synthesized by reacting magnesium hydroxide (58 g, 1 mole) with propionic acid (445 g, 6 mole), following the same procedure. Alumatrane [Al(OCH₂CH₂)₃N], titanatrane {Ti(OCH₂CH₂)₃N-[OCH₂CH₂N(CH₂CH₂OH)₂]}, and zirconium isobutyrate {Zr[O₂CCH(CH₃)₂]₂(OH)₂} were synthesized as described in previous work.^{30–32}

Sodium propionate, alumatrane, and magnesium propionate were dissolved in ethanol at a selected molar ratios to result in Na_{1.67}Al_{10.33}Mg_{0.67}O₁₇ (NAMO) composition with 50 wt.% excess sodium. The precursor solution with 3 wt.% ceramic loading was aerosolized and combusted to generate nanoparticles using the liquid-feed flame spray pyrolysis (LF-FSP) apparatus.^{30–34} Nanopowders of TiO₂ and ZrO₂ were also prepared, by aerosol combustion of titanatrane and zirconium isobutyrate, respectively.

Powder and film processing

All as-produced nanopowders (NPs) were dispersed in EtOH (200 proof, Decon Labs) with 4 wt. % bicine (Sigma-Aldrich) dispersant, using an ultrasonic horn (Vibra cell VC-505, Sonics and Materials, Inc.) at 100 W for 10 min. After 4 h of settling, the supernatant was decanted and dried. TiO₂ and ZrO₂ at selected wt. % were added to the NAMO NPs during suspension formulation. Table 1 lists target compositions of the mixed NP systems used here.

Table 2 lists components used for formulating NAMO-2TiO₂-10ZrO₂ green films, shown as a representative example. All components were added to a 20 ml vial and ball-milled with 3.0 mm diameter spherical ZrO₂ beads for 24 h to homogenize the suspension. Suspensions were cast using a wire wound rod coater (Automatic Film Applicator-1137, Sheen Instrument, Ltd.). Dried green films were manually peeled off the Mylar substrate, cut to selected sizes, and thermo-compressed at 80–100 °C with a pressure of 30–40 MPa

for 5 min using a heated bench top press (Carver, Inc.) to improve packing density.

Green films were heated to selected temperatures and dwell times in a box furnace (KSL-1700X, MTI Corporation), placed in between Al₂O₃ disks (AdValue Technology) to prevent sample warping.

Symmetrical cell construction

Symmetric cells (Na/NAMO/Na) were assembled in a fume hood under N₂ flow as a semi-inert environment. Before cell assembly, the metallic Na was scraped to expose a clean surface. Na was pressed between Mylar sheets to produce smooth and flat surfaces (0.64 cm² × 0.6 mm thick). After removing the Mylar, the Na component was rinsed briefly in methanol and hexane solutions. Symmetrical cells were constructed using a standard procedure.

Characterization

X-ray diffraction measurements were carried out using a Rigaku Rotating Anode Goniometer. Scans were made from 5 to 70° 2 θ , using Cu K α radiation (1.541 Å) operating at 40 kV and 100 mA. The Jade program 2010 (Materials Data, Inc.) was used for analysis.

Specific surface areas (SSAs) were obtained using a Micromeritics ASAP 2020 sorption analyser. Samples (300 mg) were degassed at 200 °C/5 h. Each analysis was run at –196 °C (77 K) with N₂. The SSAs were determined by the BET multipoint method using ten data points at relative pressures of 0.05–0.30. SSA was converted to average particle sizes (APS) using the equation APS = 6/(SSA \times ρ). The net density (ρ) of the as-produced NP was approximated by rule of mixtures.

Scanning electron microscopy (SEM) micrographs were taken using FEI NOVA Nanolab SEM and Philips XL-30 SEM. Powder samples were used as is, sintered films were fractured for imaging. All samples were sputter coated with Au/Pd using a SPI sputter coater.

A Q600 simultaneous TGA/DSC (TA Instruments, Inc.) was used to observe thermal decomposition of NPs and green films. Samples (15–25 mg) were loaded in alumina pans and ramped to 900 °C at 10 °C min^{–1} under constant air flow at 60 ml min^{–1}.

Final sintered film densities were determined by Archimedes method using ethanol.

Room temperature AC impedance data were collected with SP-300 (Bio-Logic LLC) in a frequency range of 7 MHz to 1 Hz. Concentric Au/Pd electrodes, 3 mm in diameter, were deposited using a SPI sputter coater on both surfaces of the films using a deposition mask. “EIS spectrum analyser” software was used for extracting total resistance. Equivalent circuit consisting of (R_{total}Q_{total})(Q_{electrode}) was used. R and Q denote resistance and constant phase element, respectively. SEM fracture surface images were taken to measure sample thicknesses.

Table 1. Compositions studied (wt.%).

	TiO ₂	ZrO ₂
NAMO	0	0
NAMO -1TiO ₂	1	0
NAMO -2TiO ₂	2	0
NAMO -2TiO ₂ -10ZrO ₂	2	10
NAMO -3TiO ₂	3	0
NAMO -3TiO ₂ -10ZrO ₂	3	10

Table 2. Suspension formulation (NAMO-2TiO₂-10ZrO₂).

	Role	Wt.%
NAMO (with bicine)	Ceramic (dispersant)	25.5
ZrO ₂ (with bicine)	Ceramic (dispersant)	2.95
TiO ₂ (with bicine)	Ceramic (dispersant)	0.58
Polyvinyl Butyral	Binder	4.69
Benzyl Butyl Phthalate	Plasticizer	4.69
Propanol	Solvent	30.9
Acetone	Solvent	30.4

Symmetrical cells were cycled using an SP-300 (Bio-Logic LLC) in a DC steady state approach where constant current was held (28 μA) and the resulting potential was measured over time.

Results and discussion

The basic objectives of the work reported here were to develop optimal methods of processing $\beta''\text{-Al}_2\text{O}_3$ thin (<100 μm), dense (> 95 %) films that also exhibit superior Na^+ conductivity, starting from

flame made NPs. We have previously demonstrated that this approach allows the processing of a number of Li^+ conducting ceramic electrolytes at similar dimensions that are otherwise difficult to process.³⁰⁻³²

To establish the best processing conditions, it is necessary to fully characterize the starting NPs produced as described in the experimental section and in previous publications. Thereafter, we characterized the sintering behavior of the processed green films with se-

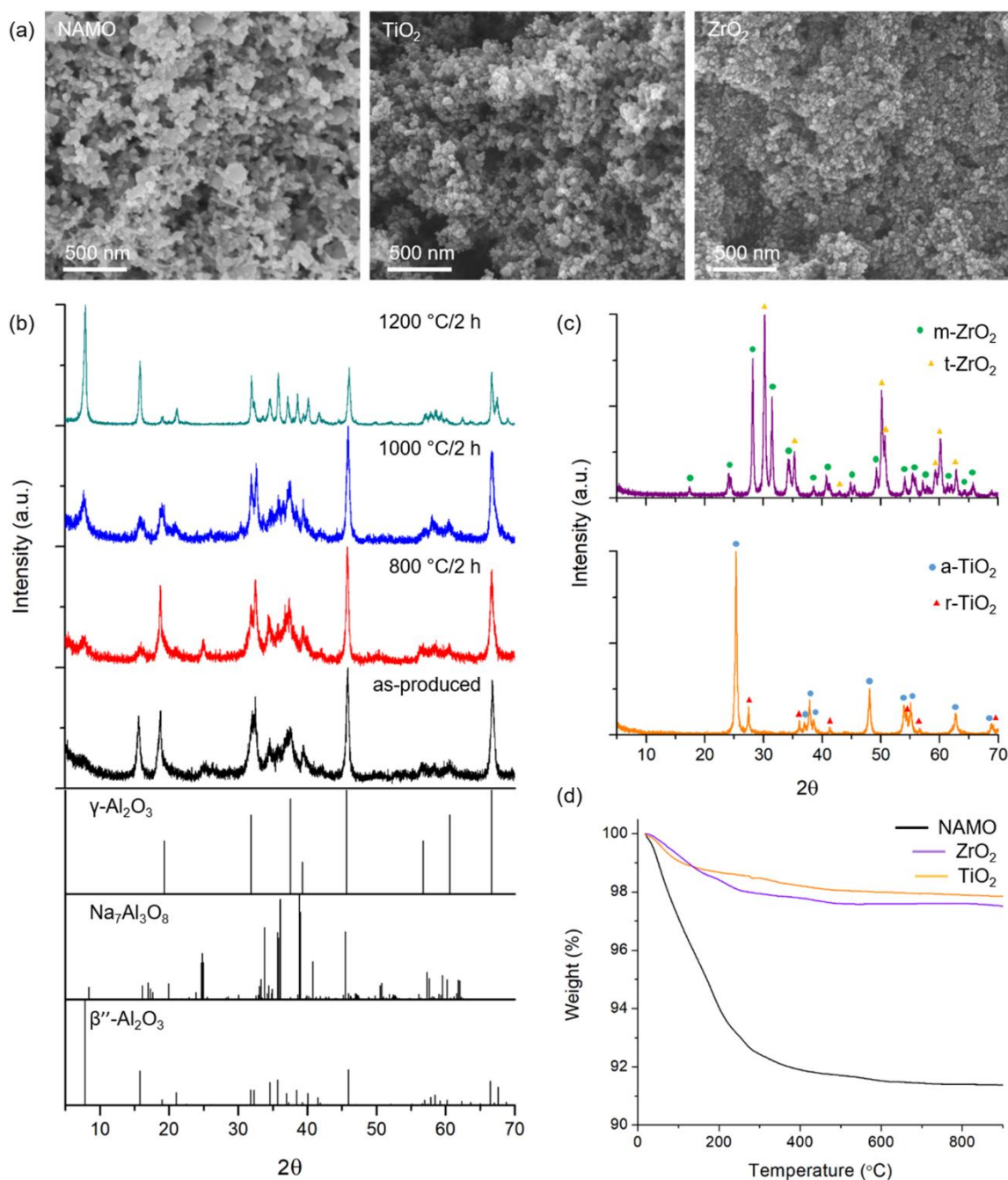


Fig. 1 (a) SEM images of as-produced NAMO, TiO_2 , and ZrO_2 NPs. (b) XRD patterns of as-produced and calcined NAMO NPs. Reference files used are $\gamma\text{-Al}_2\text{O}_3$ (PDF#: 00-050-0741), $\text{Na}_7\text{Al}_3\text{O}_8$ (PDF#: 04-009-1560), and $\beta''\text{-Al}_2\text{O}_3$ (PDF#: 01-073-9550). (c) XRD patterns of as-produced ZrO_2 and TiO_2 NPs. Reference files used are m- ZrO_2 (PDF#: 98-000-0105), t- ZrO_2 (PDF#: 04-005-4207), a- TiO_2 (PDF#: 98-000-0081), and r- TiO_2 (PDF#: 98-000-0375). (d) TGA plots of NAMO, ZrO_2 , and TiO_2 NPs.

lected wt.% of TiO_2 and ZrO_2 additions. The effects of sintering temperature and additives on the final microstructures and ionic conductivities are then compared.

Flame made nanopowders (NPs)

$\text{Na}_{1.67}\text{Al}_{10.33}\text{Mg}_{0.67}\text{O}_{17}$ (NAMO) was selected as it is one of the standard compositions used in $\beta''\text{-Al}_2\text{O}_3$ syntheses and processing. The Mg^{2+} dopant promotes $\beta''\text{-Al}_2\text{O}_3$ phase formation as excess Na is required to maintain charge neutrality. A 50% excess of Na was used to compensate for its loss during sintering. A fairly high Na content was selected given that the loss rate is much faster in thinner samples compared to thick pellets and no external Na_2O source such as a powder bed was used during sintering.³¹

As-produced NPs were characterized by SEM, XRD, BET, and TGA-DTA to confirm the particle sizes and morphologies, crystallographic phases present, and thermal stability. Fig. 1a shows SEMs of as-synthesized NPs. Specific surface areas (SSAs) obtained by BET were 52, 55, and 32 $\text{m}^2 \text{g}^{-1}$ for NAMO, TiO_2 and ZrO_2 , corresponding to average particle sizes (APSS) of 36, 28, and 32 nm, respectively. Particles show narrow particle size distribution, and rather spherical morphologies, typical of flame made NPs.

The XRD patterns of the as-produced and calcined NAMO at selected temperatures are shown in Fig. 1b. As-produced powder is a mixture of $\gamma\text{-Al}_2\text{O}_3$, $\beta''\text{-Al}_2\text{O}_3$, and $\text{Na}_7\text{Al}_3\text{O}_8$, consistent with our earlier work.²³ LF-FSP produces kinetic, rather than thermodynamic phases, due to the rapid combustion and quenching involved; thus, often times the as-produced NPs are not single phase but mixtures. Furthermore, note that the relative peak intensities of $\beta''\text{-Al}_2\text{O}_3$ are also disproportionate compared to the reference pattern. However, on heating, peaks ascribed to $\gamma\text{-Al}_2\text{O}_3$ and $\text{Na}_7\text{Al}_3\text{O}_8$ gradually grow smaller and eventually disappear at 1200 °C as they react to form $\beta''\text{-Al}_2\text{O}_3$. Single-phase $\beta''\text{-Al}_2\text{O}_3$ forms at 1200 °C and the relative peak intensities align well with the reference pattern. Fig. 1c depicts XRD patterns of as-produced ZrO_2 and TiO_2 NPs. They also show a mixture of two phases, m- ZrO_2 (monoclinic) and t- ZrO_2 (tetragonal) for ZrO_2 , and a- TiO_2 (anatase) and r- TiO_2 (rutile) for TiO_2 , typical of flame made NPs.^{33,34} a- TiO_2 converts to r- TiO_2 (>400 °C) and m- ZrO_2 converts to t- ZrO_2 (>1170 °C) far below the sintering temperatures investigated in this study as detailed below. Hence, the mixed phase in the as-produced state has no influence on sintering as the respective material becomes single phase on heating.

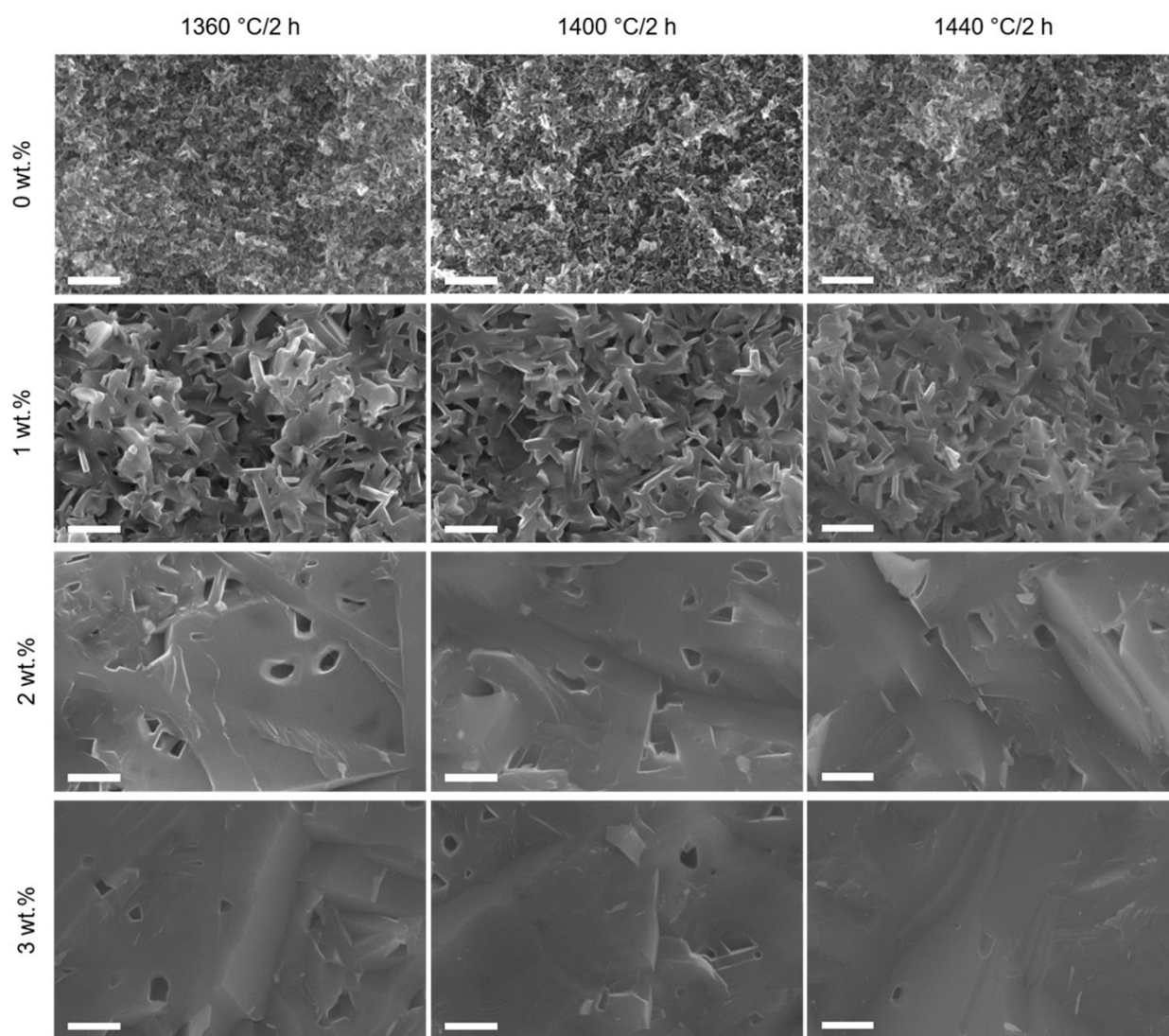


Fig. 2. SEM fracture surface images of NAMO- $x\text{TiO}_2$ ($x = 0, 1, 2, 3$) sintered to selected temperatures (Scale bar = 2 μm).

Fig. 1d illustrates TGA mass loss curves for the as-produced NPs. Most mass loss takes place <250 °C, due to physi-/chemi-sorbed water on powder surfaces. The higher mass loss of NAMO suggests its hygroscopic nature compared to TiO₂ and ZrO₂, consistent with the literature.³⁵ The absence of mass loss near the melting point of Na₂CO₃ (850 °C) indicates the as-produced powder contains no or little Na₂CO₃. DTA curves are not shown as no noticeable endo-/exothermic peaks were observed.

Effect of TiO₂ addition on the sintering behavior of NAMO

Figs. 2 and S1 compare the microstructures of the sintered NAMO with TiO₂ addition. When sintered without any additives, interconnected submicron plate-like grains are observed up to 1440 °C with limited densification. At fixed temperatures, denser microstructures are obtained with increasing TiO₂ additions. Grain sizes increase dramatically with 2 and 3 wt.% TiO₂ addition. At these wt.%, the length of some of the plate-like grains surpass the field of the SEMs whereas a number of grains are observed without TiO₂ addition, but less with 1 wt.% TiO₂.

Clearly, TiO₂ aids sintering. Indeed, Ti⁴⁺ dopant has been reported to substitute Al³⁺ thereby generating Al³⁺ vacancies which enhance Al³⁺ diffusion rates.³⁶ In addition, a number of low melting point (1030-1130 °C) TiO₂-Na₂O line compounds such as Na₄TiO₄, Na₈Ti₅O₁₄, and Na₂Ti₃O₇ likely form inducing liquid phase sintering.³⁷

High density microstructures are achieved at as low as 1360 °C/2 h. For example, NAMO with 3 wt.% TiO₂ addition sintered to 1360 °C/2 h is 98.4±1.0 % dense as determined by Archimedes method. Earlier attempts to introduce TiO₂ to NAMO have been reported, but none report sintering temperatures as low as demonstrated here. Hence, the properties of the starting powder, particularly the nanometer length scales, must be a key factor driving densification.

In Fig. 2, at a fixed TiO₂ content, higher sintering temperatures lead to denser microstructures. Also note that there are no macroscopic pores but rather *uniformly sized submicron pores due to the small and uniform particle sizes of the starting powder*. This is very important as the presence of macroscopic pores (> 10 μm) at thicknesses of < 100 μm can result in non-uniform ion transport arising

from local in-homogeneities that can form during charge/discharge cycling of a cell.

Fig. 3a compares the XRD patterns of NAMO-xTiO₂ (x= 0, 1, 2, 3) sintered to 1400 °C/2 h. β'' and β-Al₂O₃ share the majority of the peaks such that those that don't overlap and are commonly used for phase identification are labeled. All samples show mixed phases of β'' and β-Al₂O₃ at varying fractions. When comparing the peak intensities of those near 20° 2θ and 45° 2θ, the relative intensities of β''-Al₂O₃ decrease with increasing TiO₂ content, suggesting TiO₂ addition reduces β''-Al₂O₃ fraction. On another note, with increasing TiO₂ content, peaks at ~8° and ~16° 2θ intensify. These peaks correspond to (003) and (006) for β''-Al₂O₃ and (002) and (004) for β-Al₂O₃, suggesting a preferred orientation forms. Grain reorientation during liquid phase sintering, as discussed earlier, is likely the cause of preferred orientation and increasing grain sizes.

Fig. 3b traces β''-Al₂O₃ phase fractions at all tested sintering schedules. At a fixed TiO₂ doping level, higher temperatures result in lower β''-Al₂O₃ fractions. This is simply due to Na₂O loss at higher temperatures since β-Al₂O₃ has lower Na content per formula unit. At fixed temperature, increasing TiO₂ content generally results in lower β''-Al₂O₃ fraction. Literature reports TiO₂ doping stabilizes β-Al₂O₃.³⁸ However, given that the β''-Al₂O₃ fraction decreases with increasing sintering temperature at fixed TiO₂ doping level, it also appears that TiO₂ addition aids Na₂O loss at lower temperatures. It may be that Na₂O is lost from the intermediate liquid phase formed along the Na₂O-TiO₂ line compounds such that higher doping levels result in faster loss. Another possibility is that Na₂O is lost faster along the (00z) plane since increased TiO₂ doping results in higher degrees of preferred orientation and lower β''-Al₂O₃ fraction.

Effect of ZrO₂ addition on the sintering behavior of NAMO

ZrO₂ NPs at 10 wt.% were introduced to NAMO-xTiO₂ (x= 2, 3) with the object of controlling the final sintered microstructures. Secondary immiscible phases of ZrO₂ or YSZ are commonly mixed with β''-Al₂O₃ to increase the fracture toughness by mechanisms of stress induced phase transformation toughening (tetragonal to monoclinic

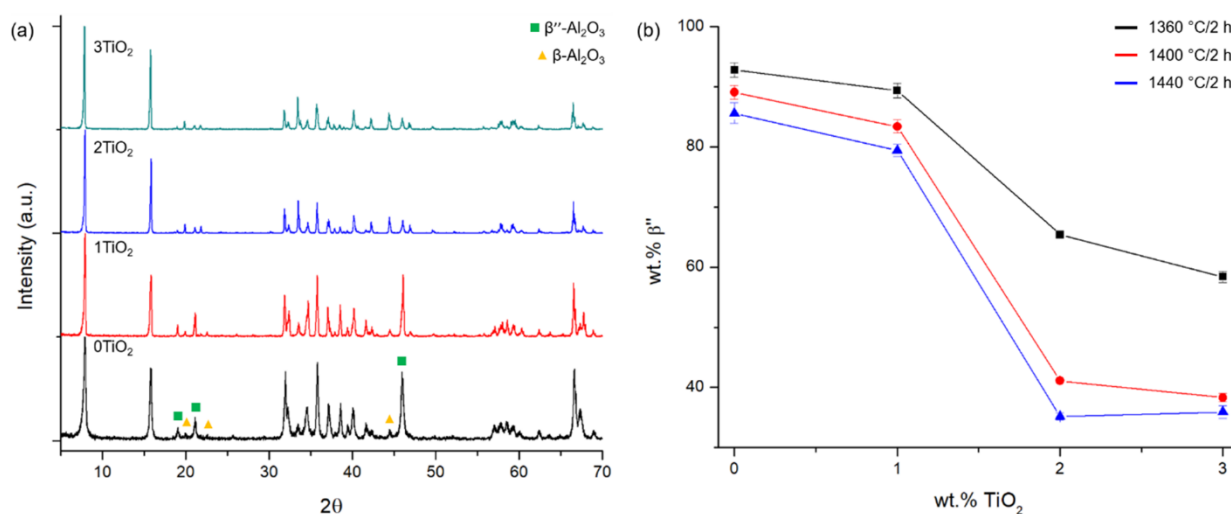


Fig. 3. (a) XRD patterns of NAMO-xTiO₂ (x= 0, 1, 2, 3) sintered to 1400 °C/2 h. Reference files used are β''-Al₂O₃ (PDF#: 01-073-9550) and β-Al₂O₃ (PDF#: 01-073-9548). Peaks that do not overlap and are commonly used for differentiating β''/β-Al₂O₃ are labeled. (b) Trace of β''-Al₂O₃ fraction of sintered NAMO-xTiO₂ (x= 0, 1, 2, 3).

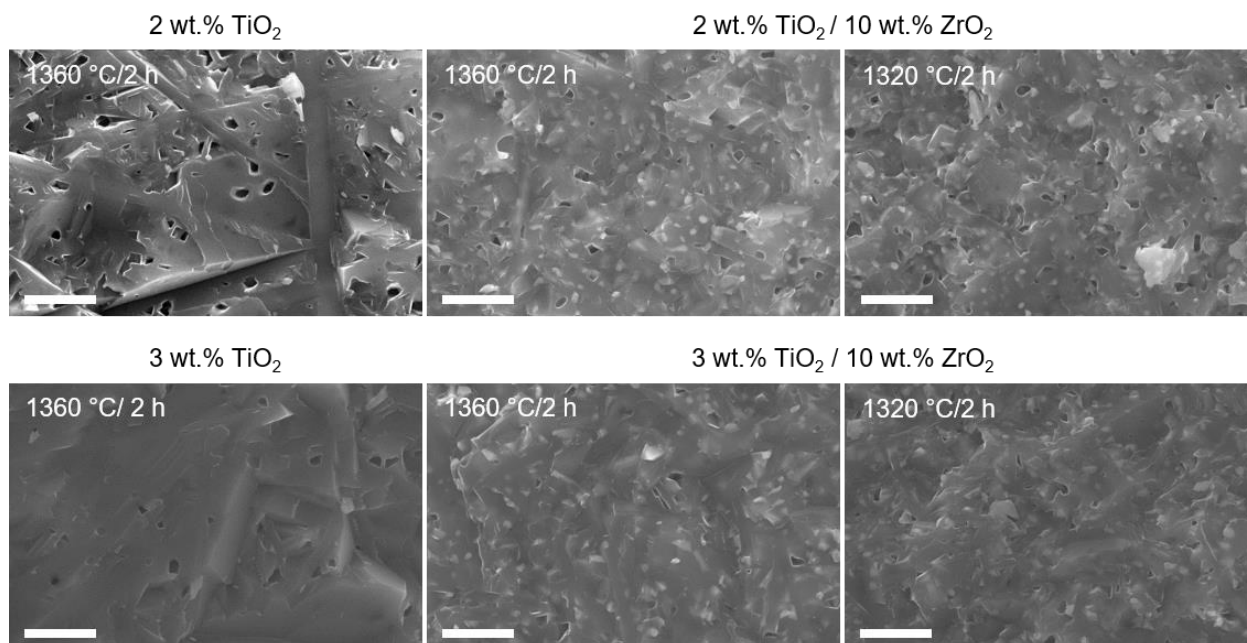


Fig. 4. SEM fracture surface images of sintered NAMO- $x\text{TiO}_2$ -10ZrO₂ ($x=2, 3$) (Scale bar = 5 μm).

ZrO₂) and crack deflection. ZrO₂ addition also promotes densification of β'' -Al₂O₃ which in turn can increase the β'' -Al₂O₃ fraction as less Na₂O is lost at lower sintering temperatures or due to faster pore closure thereby reducing sample surface areas.¹² Furthermore, ZrO₂ can pin grain boundaries and prohibit grain growth resulting in smaller, more equiaxed grain sizes. Briefly, ZrO₂ addition is an efficient method to produce strong and tough materials and has been studied extensively. However, since ZrO₂ does not conduct Na⁺, excessive addition results in higher resistances. A significant conductivity drop has been reported when > 10 wt.% ZrO₂ was introduced.³⁹

Figs. 4 and S2 compare SEM fracture surfaces of the sintered NAMO- $x\text{TiO}_2$ -10ZrO₂ ($x=2, 3$). With ZrO₂ addition, high density microstructures can be achieved at as low as 1320 °C/2 h. Compared to

samples sintered without added ZrO₂; no large grains are observed, suggesting ZrO₂ successfully inhibits grain growth. The majority of the ZrO₂ grains are 400-600 nm and are well distributed within the β'' -Al₂O₃ matrix providing uniform properties throughout the material.

XRD patterns of the NAMO- $x\text{TiO}_2$ ($x=2, 3$) and NAMO- $x\text{TiO}_2$ -10ZrO₂ ($x=2, 3$) sintered to 1360 °C/2 h are compared in Fig. 5. Samples with ZrO₂ show both monoclinic and tetragonal ZrO₂ present at 2-3 wt.% and 9-10 wt.%, respectively. Part of the introduced Ti⁴⁺ seems to have diffused into ZrO₂, stabilizing the tetragonal phase.⁴⁰ Comparing NAMO-2TiO₂ and NAMO-2TiO₂-10ZrO₂, the peak intensities of β'' -Al₂O₃ relative to β -Al₂O₃ substantially increase with ZrO₂

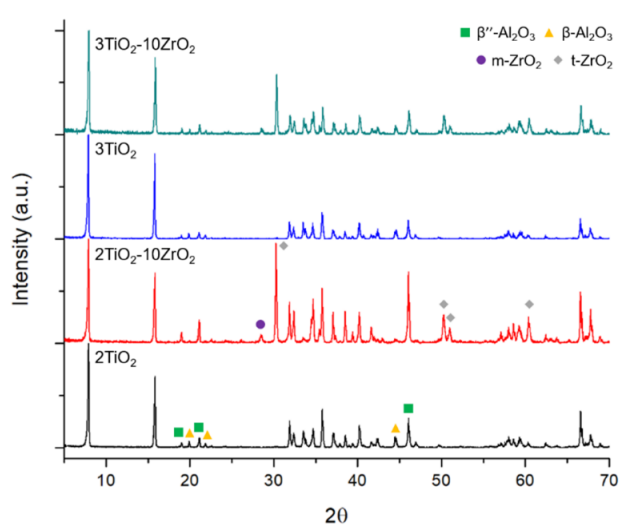


Fig. 5. XRD patterns of NAMO- $x\text{TiO}_2$ ($x=2, 3$) and NAMO- $x\text{TiO}_2$ -10ZrO₂ ($x=2, 3$) sintered to 1360 °C/2 h. Reference files used are β'' -Al₂O₃ (PDF#: 01-073-9550), β -Al₂O₃ (PDF#: 01-073-9548), m-ZrO₂ (PDF#: 98-000-0105), and t-ZrO₂ (PDF#: 04-005-4207).

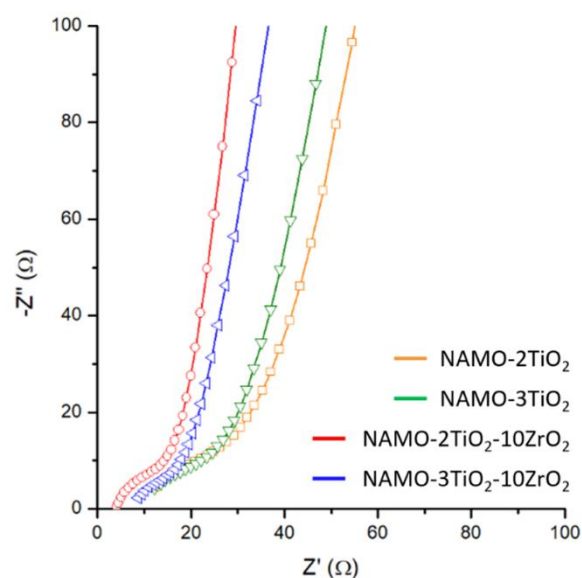
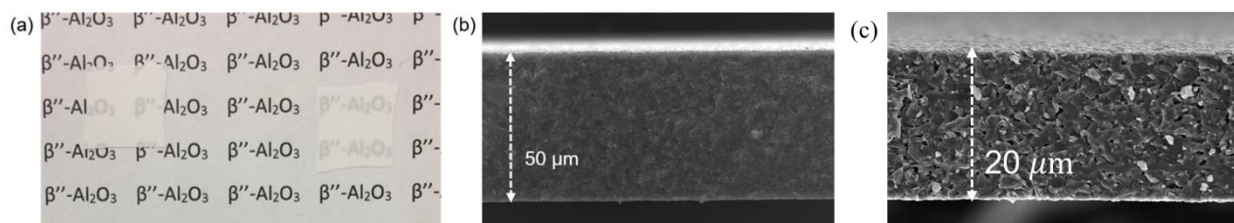


Fig. 6. Nyquist plots of NAMO- $x\text{TiO}_2$ ($x=2, 3$) and NAMO- $x\text{TiO}_2$ -10ZrO₂ ($x=2, 3$) sintered to 1360 °C/2 h (sample thickness= 50 μm).

Table 3. Summary of physical and electrochemical properties of high density films.

	Sintering schedule	Density [g cm ⁻³]	Relative density [%]	σ_{RT} [mS cm ⁻¹]	β'' fraction [wt.%]
NAMO-2TiO ₂	1360 °C/2 h	3.07±0.02	93.8±0.6	2.2±0.4	65.4±0.9
NAMO-2TiO ₂ -10ZrO ₂	1360 °C/2 h	3.34±0.04	96.0±1.1	4.1±0.7	82.3±0.9
	1320 °C/2 h	3.32±0.02	95.5±0.7	5.4±0.9	83.5±0.9
NAMO-3TiO ₂	1360 °C/2 h	3.23±0.03	98.4±1.0	2.7±0.1	58.4±0.9
NAMO-3TiO ₂ -10ZrO ₂	1360 °C/2 h	3.40±0.02	98.4±0.7	3.7±0.2	61.0±0.9
	1320 °C/2 h	3.33±0.03	96.5±0.9	3.3±0.1	70.0±0.8

**Fig. 7** (a) Optical image of 1320 °C/2 h sintered NAMO-2TiO₂-10ZrO₂. Samples are roughly 2 x 2 cm². (b) SEM fracture surface image of 1320 °C/2 h sintered NAMO-2TiO₂-10ZrO₂ (50 μm thick). (c) Fracture surface of 20 μm thick film.

addition. Preferred orientation attenuates as well, as evidenced by weaker relative peak intensities for peaks at $\sim 8^\circ$ and $\sim 16^\circ$ 2 θ compared to others. A similar trend is not observed for the 3 wt. % TiO₂ counterpart. It appears ZrO₂ hosts TiO₂ and at 3 wt.% TiO₂, the amount of TiO₂ is still enough to induce preferred orientation through liquid phase sintering but no large grains were observed.

Ionic conductivities

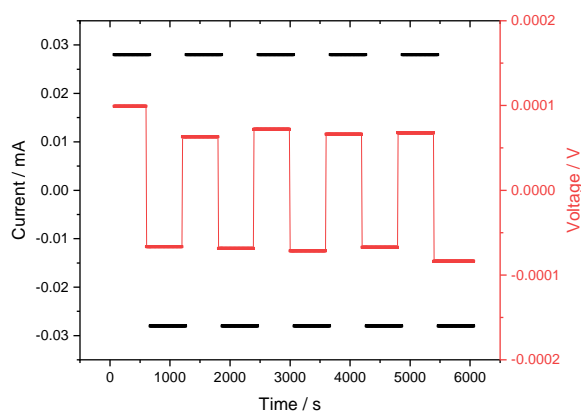
Table 3 compares the relative densities, ionic conductivities, and β'' -Al₂O₃ fractions of high density samples. Detailed phase compositions are listed in Table S1. Fig. 6 presents Nyquist plots of NAMO-xTiO₂ (x= 2, 3) and NAMO-xTiO₂-10ZrO₂ (x=2, 3) sintered to 1360 °C/2 h. All compositions show high conductivities > 1 mS cm⁻¹. Among them, the conductivities of NAMO-2TiO₂ and NAMO-3TiO₂ sintered to 1360 °C/2 h are on the lower end likely due to lower relative density and β'' -Al₂O₃ fraction, respectively. NAMO-2TiO₂-10ZrO₂ sintered to 1320 and 1360 °C/2 h show the highest ionic conductivities of 4-6 mS cm⁻¹ as a result of high relative densities combined with high β'' -Al₂O₃ fraction. Note 10-12 wt.% ZrO₂ is present, based on

XRD, and hence a very low β -Al₂O₃ fraction. NAMO-3TiO₂-10ZrO₂ sintered to 1320 and 1360 °C/2 h offers slightly lower conductivities of 3-4 mS cm⁻¹ likely due to lower β'' -Al₂O₃ fraction. No reports on room temperature β'' -Al₂O₃ conductivity are available, but the obtained conductivities are 3-6 fold higher compared to the ambient conductivity of polycrystalline β -Al₂O₃.⁶

Fig. 7a is an optical image of typical dense sintered films produced in this study with dimensions of $\sim 2 \times 2$ cm². Translucency is a result of high density and low thickness. All dense samples had sintered thicknesses ranging from 20-70 μm, Figs. 7b and 7c.

Fig. 8 shows a Na/NAMO-2TiO₂-10ZrO₂/Na symmetrical cell galvanostatically cycled at room temperature. The cells were cycled using a DC steady state method in which a constant current (28 μA or 44 μA cm⁻²) was held and the resulting potential was measured over time. A DC conductivity value of 4.2 mS cm⁻¹ was calculated (V= 0.07 mV, sample thickness= 68 μm, area= 0.64 cm²), in good agreement with the AC impedance measurement results.

Thus, we have demonstrated the potential of these materials to meet the conductivity, mechanical and thickness requirements needed to construct Na batteries utilizing solid-state electrolytes.

**Fig. 8.** Galvanostatic cycling of Na/NAMO-2TiO₂-10ZrO₂/Na symmetric cell at the current density of 44 μA cm⁻².

Conclusions

Through compositional control of flame made nanopowders, we have identified conditions whereby β'' -Al₂O₃ sintering temperatures can be reduced by nearly 300 °C compared to conventional approaches. Increasing TiO₂ dopant levels dramatically enhances sintering but at the cost of excessive grain growth. However, introducing a secondary immiscible phase, ZrO₂, provides excellent microstructural control. Sintered films 20-70 μm thick, 96-98% dense with 60-85 wt.% of β'' -Al₂O₃ fractions can be produced using the approach developed here. The combination of high densities and high β'' -Al₂O₃ fractions results in room temperature ionic conductivities of 3-6 mS cm⁻¹ in these thin films. The formation of *t*-ZrO₂ points to the potential for robust mechanical properties.

Finally, we demonstrate a symmetrical Na/ β'' -Al₂O₃/Na cell that can be cycled at ambient showing its potential utility in Na batteries using β'' -Al₂O₃ solid electrolytes.

The processes used are easily translatable to mass production, and with the availability of β'' -Al₂O₃ thin films, novel battery designs in flat geometries can be realized perhaps providing an obvious pathway to Na solid state batteries that operate at ambient temperatures.

The main focus of the work has been on optimizing compositions and sintering conditions of NAMO. Future work will address mechanical properties, critical current densities, conductivity measurements at varying temperatures, and construction of Na batteries using the NAMO films.

Acknowledgements

We thank the start-up company, Na4B for a subcontract on their Phase II NSF grant from DMR for early support of this work. We thank Mercedes Benz Research and Development North America for a generous gift that funded the major part of this work.

Notes and references

1. J.H. Kennedy and A.F. Sammells, *J. Electrochem. Soc.*, 1972, **119**, 1609.
2. M.S. Whittingham, *J. Chem. Phys.*, 1971, **54**, 414.
3. R.C. De Vries and W.L. Roth, *J. Am. Ceram. Soc.*, 1969, **52**, 364.
4. J.H. Kennedy, J.R. Akridge and M. Kleitz, *Electrochim. Acta*, 1979, **24**, 781.
5. T. Oshima, M. Kajita and A. Okuno, *Int. J. Appl. Ceram. Technol.*, 2004, **1**, 269.
6. X. Lu, G. Xia, J.P. Lemmon and Z. Yang, *J. Power Sources*, 2010, **195**, 2431.
7. V. Palomares, P. Serras, I. Villaluenga, K.B. Hueso, J. Carretero-Gonzalez and T. Rojo, *Energy Environ. Sci.*, 2012, **5**, 5884.
8. R. Benato, N. Cosciani, G. Crugnola, S.D. Sessa, G. Lodi, C. Parmeggiani and M. Todeschini, *J. Power Sources*, 2015, **293**, 127.
9. T.K. Hunt and N. Weber and T. Cole, *Solid State Ionics*, 1981, **5**, 263.
10. T. Cole, *Science*, 1983, **221**, 915.
11. S. Mekhilef, R. Saidur and A. Safari, *Renew. Sustain. Energy Rev.*, 2012, **16**, 981.
12. Y. Sheng, P. Sarkar and P. S. Nicholson, *J. Mater. Sci.* 1988, **23**, 958.
13. N.L. Canfield, J.Y. Kim, J.F. Bonnett, R.L. Pearson, V.L. Sprenkle, and K. Jung, *Mater. Sci. Eng. B*, 2015, **197**, 43.
14. L.-P. Yang, S.-J. Shan, X.-L. W., X.-M. Liu, H. Yang and X.-D. Shen, *Ceram. Internat.*, 2014, **40**, 9055.
15. S. Barison, S. Fasolin, C. Mortalò, S. Boldrini and M. Fabrizio, *J. Europ. Ceram. Soc.*, 2015, **35**, 2099.
16. E. Mercadelli, A.S. Arico, A. Gondolini, S. Siracusano, M. Ferraro, V. Antonucci and A. Sanson, *J. Alloys Compd.* 2017, **696**, 1080.
17. R. Subasri, T. Mathews, O.M. Sreedharan and V. S. Raghunathan, *Solid State Ionics*, 2003 **158**, 199.
18. J. Wang, X.-P. Jiang, X.-L. Wei, H. Yang and X.-D. Shen, *J. Alloys Compd.*, 2010, **497**, 295.
19. A. Mali and A. Petric, *J. Europ. Cer. Soc.* 2012, **32**, 1229.
20. N. Li, Z. Wen, Y. Liu, X. Xu, J. Lin, Z. Gu, *J. Europ. Cer. Soc.*, 2009, **29**, 3031.
21. X. Wei, Y. Cao, L. Lu, H. Yang and X. Shen, *J. Alloys Compd.*, 2011, **509**, 6222.
22. S.-J. Shan, L.-P. Yang, X.-M. Liu, X.-L. Wei, H. Yang and X.-D. Shen, *J. Alloys Compd.*, 2013, **563**, 176.
23. A.C. Sutorik, S.S. Neo, T. Hinklin, R. Baranwal, D.R. Treadwell, R. Narayanan and R.M. Laine, *J. Am. Ceram. Soc.* 1998, **81**, 1477.
24. A. Mali and A. Petric, *J. Power Sources*, 2011, **196**, 5191.
25. D. La Rosa, G. Monforte, C. D'Urso, V. Baglio, V. Antonucci, A.S. Aric, *ChemSusChem*, 2010, **3**, 1390.
26. D. Reed, G. Coffey, E. Mast, N. Canfield, J. Mansurov, X. Lu, V. Sprenkle, *J. Power Sources*, 2013, **227**, 94.
27. G.E. Youngblood, G.R. Miller and R.S. Gordon, *J. Am. Ceram. Soc.*, 1978, **61**, 86.
28. A. V. Virkar, J.-F. Jue and K.-Z. Fung, *U.S. Patent*, 6117807A.
29. L. Liu, X. Qi, Q. Ma, X. Rong, Y.-S. Hu, Z. Zhou, H. Li, X. Huang and L. Chen, *ACS Appl. Mater. Interfaces*, 2016, **8**, 32631.
30. E. Yi, W. Wang, S. Mohanty, J. Kieffer, R. Tamaki and R. M. Laine, *J. Power Sources*, 2014, **269**, 577.
31. E. Yi, W. Wang, J. Kieffer and R. M. Laine, *J. Mater. Chem. A*, 2016, **4**, 12947.
32. E. Yi, W. Wang, J. Kieffer and R. M. Laine, *J. Power Sources*, 2017, **352**, 156.
33. C.R. Bickmore, K.F. Waldner, R. Baranwal, T. Hinklin, D.R. Treadwell and R.M. Laine, *J. Europ. Ceram. Soc.* 1998, **18**, 287.
34. M. Kim and R.M. Laine, *J. Am. Ceram. Soc.* 2010, **93**, 709.
35. F. Harbach, *Solid State Ionics*, 1983, **9&10**, 231.
36. H. Erkalfa, Z. Misirli and T. Baykara, *Ceram. Int.*, 1998, **24**, 81.
37. G. Eriksson and A. D. Pelton, *Metall. Mater. Trans. B*, 1993, **24B**, 795.
38. S.-J. Shan, L.-P. Yang, X.-M. Liu, X.-L. Wei, H. Yang and X.-D. Shen, *J. Alloys Compd.*, 2013, **563**, 176.
39. X. Lu, J. P. Lemmon, V. Sprenkle and Z. Yang, *JOM*, 2010, **62**, 31.
40. C.-S. Hwang, S.-C. Tsaur and Y.-J. Chang, *J. Ceram. Soc. Jpn.*, 1994, **102**, 1111.
- 41.